



Cite this: *Chem. Commun.*, 2025, 61, 1395

Received 30th September 2024,
Accepted 9th December 2024

DOI: 10.1039/d4cc05101g

rsc.li/chemcomm

Concave Fe₂O₃ nanocubes with high-index facets for ammonia production from electrocatalytic nitrate reduction†

Yuwei Zhang,^a Mingyang Xu,^a Jiaxin Zhou,^a Fen Yao^b and Hanfeng Liang^{id} ^{*a}

An iron oxide catalyst with high-index (13–44) and (12–38) facets achieves a high faradaic efficiency of 96.54% and a production rate of 1.13 mmol h^{−1} cm^{−2} towards electrocatalytic nitrate reduction to ammonia at 250 mA cm^{−2}.

Ammonia (NH₃) is an essential chemical feedstock extensively utilized in the industrial production of fertilizers and other chemicals.¹ Additionally, it shows promise as a carbon-free energy carrier, potentially replacing fossil fuels. Currently, the predominant method for industrial ammonia production is the Haber–Bosch process (H₂ + N₂ → NH₃), which operates at high temperatures (300–500 °C) and pressures (15–35 MPa), consuming significant energy.^{2,3} An alternative solution is the electrocatalytic nitrogen reduction reaction, which utilizes electricity to drive the conversion of N₂ to NH₃ under ambient conditions.^{4,5} Unfortunately, due to the challenge of breaking the extremely stable N≡N bond (941 kJ mol^{−1}), NRR suffers from low ammonia faradaic efficiency and yield, significantly limiting its potential for large-scale industrial application.⁶ In contrast, electrocatalytic nitrate reduction reaction (NtrRR) is thermodynamically more feasible because the breaking of the N–O bond requires a much lower energy input (204 kJ mol^{−1}).^{6,7} Meanwhile, soluble nitrate is widely present in industrial and agricultural effluents, causing significant environmental pollution.⁸ Therefore, converting nitrate into high value-added ammonia is crucial for both environmental protection and energy utilization.

However, the kinetics of NtrRR remain slow due to the complexity of the multi-electron coupled multi-proton transfer process. Additionally, the various reaction pathways leading to

different products (*e.g.*, NH₃, NO₂, N₂ and NO_x) reduce the selectivity for the desired ammonia products.⁹ As a result, efforts have been focused on developing NtrRR electrocatalysts with high activity and selectivity. Currently, noble metal-based catalysts (such as Ru and Pd) demonstrate superior NtrRR performance,^{10–12} but their high cost and limited availability restrict their use in large-scale applications. In this context, non-noble metals such as Cu, Co, and Fe are promising alternatives,^{13–15} though their performance needs further improvement.

Since electrocatalytic reactions occur on or near the catalysts' surface, the surface atomic arrangement (*i.e.*, the crystal facets) plays a crucial role in determining catalytic activity. Specifically, nanocatalysts with high-index facets often exhibit superior catalytic performance compared to their low-index counterparts.^{16,17} Indeed, numerous electrocatalysts with well-engineered high-index facets have been developed for both the oxygen evolution reaction (OER)^{18–20} and hydrogen evolution reaction (HER).^{18,21} However, the exploration of NtrRR electrocatalysts with high-index facets remains rare, with most examples primarily focusing on noble metal catalysts.²²

In this work, we systematically investigated the NtrRR performance of Fe₂O₃ electrocatalysts with different crystal facets. We found that the octagonal Fe₂O₃ with high-index (13–44) and (12–38) facets (H_o-Fe₂O₃) exhibits outstanding NtrRR performance, achieving a high NH₃ faradaic efficiency of up to 96.54% and a production rate of 1.13 mmol h^{−1} cm^{−2} at 250 mA cm^{−2}, outperforming most previously reported non-noble metal NtrRR catalysts. Furthermore, we assembled a “batterolyzer” by coupling the anodic N₂H₄ oxidation reaction and cathodic NtrRR, following a concept previously developed by our group.²³ This batterolyzer combines the features of a traditional battery and electrolyzer, concurrently generating electricity (with a peak power density of 2.85 mW cm^{−2}) and high-value ammonia.

We synthesized H_o-Fe₂O₃ catalysts with high-index (13–44) and (12–38) facets using a recipe we previously developed.²⁴ For comparison, we also synthesized Fe₂O₃ cubes with low-index (10–12) facets (L_c-Fe₂O₃)²⁵ and octahedra with low-index (10–14)

^a State Key Laboratory of Physical Chemistry of Solid Surfaces, College of Chemistry and Chemical Engineering, Xiamen University, China. E-mail: hfliang@xmu.edu.cn

^b Key Laboratory of Preparation and Applications of Environmentally Friendly Material of the Ministry of Education, College of Chemistry, Jilin Normal University, China

† Electronic supplementary information (ESI) available. See DOI: <https://doi.org/10.1039/d4cc05101g>

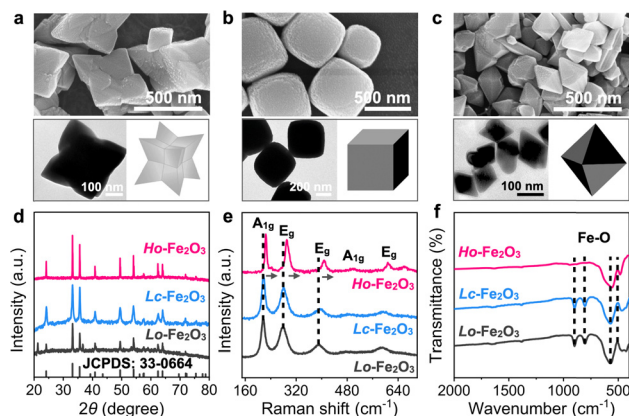


Fig. 1 Physical characterizations of the Fe_2O_3 catalysts. SEM, TEM images and structure illustrations of (a) $\text{Ho-Fe}_2\text{O}_3$, (b) $\text{Lc-Fe}_2\text{O}_3$, and (c) $\text{Lo-Fe}_2\text{O}_3$. (d) XRD patterns, (e) Raman spectra and (f) FTIR spectra of the three catalysts.

facets ($\text{Lo-Fe}_2\text{O}_3$)²⁶ using a reported wet chemical method (see details in ESI†). Scanning electron microscopy (SEM) images show the three catalysts have well-defined morphologies (Fig. 1a–c). Transmission electron microscopy (TEM) images reveal that the average particle sizes of $\text{Ho-Fe}_2\text{O}_3$, $\text{Lc-Fe}_2\text{O}_3$, and $\text{Lo-Fe}_2\text{O}_3$ are about 200, 300, and 100 nm, respectively. X-ray diffraction (XRD) analysis suggests that the diffraction peaks of the synthesized Fe_2O_3 with different exposed facets align with those of hematite (JCPDS no. 33-0664). Raman

spectra further confirm the successful synthesis of the three Fe_2O_3 catalysts (Fig. 1e). In addition, the Raman peaks of $\text{Ho-Fe}_2\text{O}_3$ shift to higher wavenumber, indicating the presence of strain and stress due to the high-index facets.²⁷ Fourier transform infrared spectroscopy (FTIR) spectra also reveal that all the characteristic peaks can be attributed to Fe_2O_3 (Fig. 1f).

We investigated the NtrRR performance of the three electrocatalysts. Given that NtrRR generates additional hydroxyl groups, thereby alkalizing the electrolyte, we selected 1 M KOH as the supporting electrolyte. We first assessed the NtrRR activity of $\text{Ho-Fe}_2\text{O}_3$ along with $\text{Lc-Fe}_2\text{O}_3$ and $\text{Lo-Fe}_2\text{O}_3$ controls, using stabilized polarization curves in 1 M KOH electrolyte with and without 0.1 M KNO_3 . No significant HER is observed for $\text{Ho-Fe}_2\text{O}_3$, $\text{Lc-Fe}_2\text{O}_3$ and $\text{Lo-Fe}_2\text{O}_3$ (Fig. 2a). Notably, $\text{Ho-Fe}_2\text{O}_3$ catalysts require only -0.145 V vs. RHE to initiate NtrRR, which is much lower than that of $\text{Lc-Fe}_2\text{O}_3$ and $\text{Lo-Fe}_2\text{O}_3$ catalysts (-0.225 and -0.194 V vs. RHE, respectively, Fig. 2b). Tafel plots further reveal the fastest NtrRR kinetics on $\text{Ho-Fe}_2\text{O}_3$, indicated by the smallest slope (66.93 mV dec^{-1} , Fig. 2c). To exclude the impact of surface area, we performed cyclic voltammetry (CV) tests within non-faradaic regions and calculated the double layer capacitances (C_{dl} , Fig. S2, ESI†). The results reveal that the three catalysts have very similar C_{dl} values, and thus similar electrochemically active surface areas (ECSA). This indicates that the different exposure of crystal facets, rather than the surface area, primarily accounts for the varying NtrRR activities.

We then conducted a 7200 s chronopotentiometry test at 250 mA cm^{-2} (Fig. S3, ESI†) and subsequently evaluated the

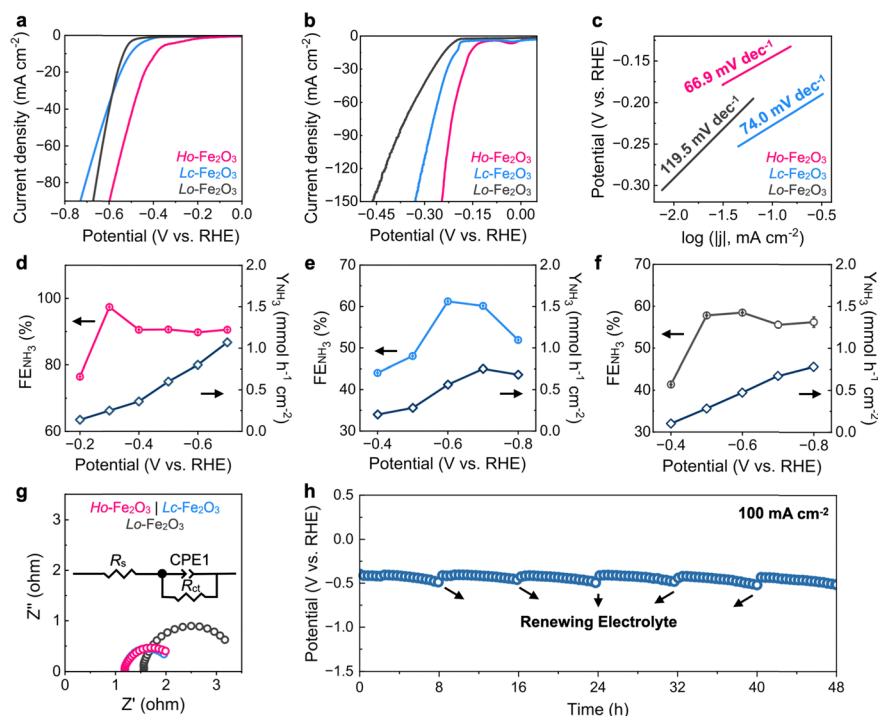


Fig. 2 Electrocatalytic NtrRR performance. (a) Polarization curves in 1 M KOH (with IR correction). (b) Polarization curves in 1 M KOH/0.1 M KNO_3 (with IR correction) and (c) the derived Tafel plots of the three catalysts. (d)–(f) Ammonia faradaic efficiencies of (d) $\text{Ho-Fe}_2\text{O}_3$, (e) $\text{Lc-Fe}_2\text{O}_3$ and (f) $\text{Lo-Fe}_2\text{O}_3$ in 1 M KOH/0.1 M KNO_3 mixed electrolyte. (g) EIS spectra of the three catalysts. (h) Chronopotentiometry curves of the $\text{Ho-Fe}_2\text{O}_3$ catalyst at 100 mA cm^{-2} in 1 M KOH/0.1 M KNO_3 mixed electrolyte.

ammonia production efficiency using ion chromatography (IC) (see ammonia and nitrate standard curves in Fig. S4, ESI†). The $\text{H}_\text{o}\text{-Fe}_2\text{O}_3$ catalysts exhibit superb faradaic efficiency (96.54%, Fig. S5a, ESI†) and ammonia yield ($1.13 \text{ mmol h}^{-1} \text{ cm}^{-2}$, Fig. S5b, ESI†), whereas $\text{L}_\text{c}\text{-Fe}_2\text{O}_3$ and $\text{L}_\text{o}\text{-Fe}_2\text{O}_3$ show lower faradaic efficiencies (75.98% and 72.11%) and ammonia yields (0.89 and $0.84 \text{ mmol h}^{-1} \text{ cm}^{-2}$). This evidence suggests that $\text{H}_\text{o}\text{-Fe}_2\text{O}_3$ exposing high-index facets not only enhances NO_3^- adsorption and activation but also effectively improves ammonia faradaic efficiency and yield rate. Notably, the three catalysts produced negligible nitrite byproducts during the chronopotentiometry tests. Specifically, the nitrite faradaic efficiencies of the $\text{H}_\text{o}\text{-Fe}_2\text{O}_3$, $\text{L}_\text{c}\text{-Fe}_2\text{O}_3$ and $\text{L}_\text{o}\text{-Fe}_2\text{O}_3$ catalysts were only 3.01%, 3.66% and 4.61%, respectively (Fig. S5a, ESI†). Overall, the NtrRR performance of $\text{H}_\text{o}\text{-Fe}_2\text{O}_3$ catalysts significantly outperforms the vast majority of recently reported NtrRR catalysts (Table S1, ESI†).

In addition to the chronopotentiometry tests, we also performed chronoamperometry tests (Fig. S6a–c, ESI†) to further investigate the effect of reaction potential on NtrRR faradaic efficiency and ammonia yield rate (Fig. 2d–f). The ammonia faradaic efficiency of the $\text{H}_\text{o}\text{-Fe}_2\text{O}_3$ catalyst remains consistently above 90% from -0.3 to -0.7 V vs. RHE (Fig. 2d). More importantly, at -0.7 V vs. RHE , the $\text{H}_\text{o}\text{-Fe}_2\text{O}_3$ catalyst achieves a high ammonia yield rate of $1.07 \text{ mmol h}^{-1} \text{ cm}^{-2}$. In contrast, the faradaic efficiencies of the $\text{L}_\text{o}\text{-Fe}_2\text{O}_3$ and $\text{L}_\text{c}\text{-Fe}_2\text{O}_3$ catalysts for ammonia production are below 60%, and their ammonia yield rates are less than $1 \text{ mmol h}^{-1} \text{ cm}^{-2}$ (Fig. 2e and f). These results indicate that the $\text{H}_\text{o}\text{-Fe}_2\text{O}_3$ catalyst maintains the highest intrinsic NtrRR activity for ammonia production among the three catalysts, suggesting that the high-index facets of $\text{H}_\text{o}\text{-Fe}_2\text{O}_3$ optimize the adsorption and reaction of intermediates for NtrRR. In addition, we measured the electrochemical impedance spectra (EIS), which show that both $\text{H}_\text{o}\text{-Fe}_2\text{O}_3$ and $\text{L}_\text{o}\text{-Fe}_2\text{O}_3$ exhibit lower impedance (Fig. 2g and Table S2, ESI†), indicating faster electron transfer, consistent with the Tafel results. The $\text{H}_\text{o}\text{-Fe}_2\text{O}_3$ catalysts could stably produce ammonia at 100 mA cm^{-2} for at least 48 h (Fig. 2h). Notably, no hydrogen production was observed during this process, and the decreased potential could be restored by renewing the electrolyte.

All three catalysts exhibit decent stability over long-term tests (Fig. 2h and Fig. S7, ESI†). We further conducted a series of physical characterization studies to examine their structural stability. SEM images reveal no significant changes in bulk morphology, although the surfaces of the catalysts appear smoother after NtrRR, suggesting slight surface reconstruction (Fig. S8, ESI†). However, XRD analysis (Fig. 3a and Fig. S9, ESI†) indicates that the phase composition remains unchanged for all three catalysts, explaining their outstanding stability. Additionally, the Fe 2p X-ray photoelectron spectroscopy (XPS) spectra of the catalysts after long-term stability tests are nearly identical to those of pristine samples (Fig. 3b and Fig. S10, ESI†). We further collected the LSV curve of $\text{H}_\text{o}\text{-Fe}_2\text{O}_3$ after stability test, which shows that the activity of $\text{H}_\text{o}\text{-Fe}_2\text{O}_3$ barely changes (Fig. S11, ESI†). These results again demonstrate that

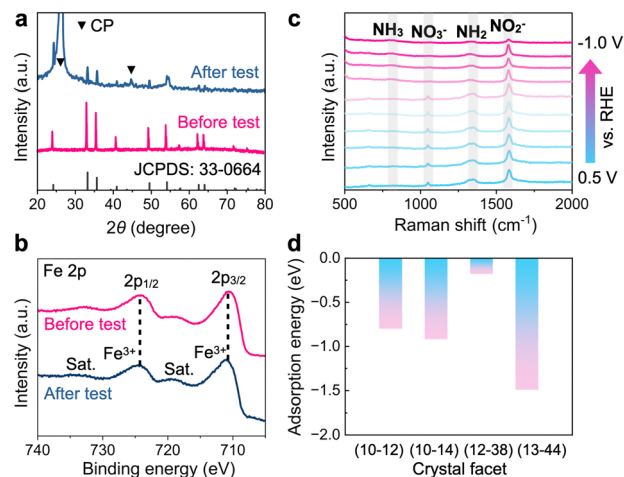


Fig. 3 (a) XRD pattern, and (b) Fe 2p XPS spectrum of $\text{H}_\text{o}\text{-Fe}_2\text{O}_3$ after long-term stability tests. (c) *In situ* Raman spectra of $\text{H}_\text{o}\text{-Fe}_2\text{O}_3$ at various potentials. (d) Adsorption energy of different crystal facets for NO_3^- .

the exposure of Fe_2O_3 to different crystal facets is the primary factor affecting its NtrRR performance.

To further investigate the NtrRR reaction pathway on $\text{H}_\text{o}\text{-Fe}_2\text{O}_3$, we performed *in situ* Raman tests. The evolution of Raman peaks indicates the disappearance of the characteristic peaks of NO_3^- , along with the appearance of the characteristic peaks of NO_2^- , NH_2 , and NH_3 as the applied potential gradually decreases from 0.5 to -1.0 V vs. RHE (Fig. 3c). Thus, the reaction pathway likely follows $\text{NO}_3^- \rightarrow \text{NO}_2^- \rightarrow \text{NH}_2 \rightarrow \text{NH}_3$, which has been observed in NtrRR on various catalysts.^{28–30} *In situ* EIS analysis reveals that $\text{H}_\text{o}\text{-Fe}_2\text{O}_3$ exhibits a smaller phase angle than $\text{L}_\text{o}\text{-Fe}_2\text{O}_3$ and $\text{L}_\text{c}\text{-Fe}_2\text{O}_3$ under the same bias, indicating that more charges participated in the redox reaction (Fig. S12, ESI†). To better understand the role of crystal facets, we conducted theoretical simulations. Previous studies suggest that the adsorption of NO_3^- is a crucial step that directly determines the NtrRR performance.^{22,31} We calculated the adsorption energies of NO_3^- on different crystal facets of Fe_2O_3 (Fig. 3d). The result shows that the (13–44) has the most negative value of -1.488 eV , followed by (10–14) and (10–12). Such favourable adsorption would promote the reaction kinetics, leading to enhanced NtrRR activity of $\text{H}_\text{o}\text{-Fe}_2\text{O}_3$.

We further assembled a batteryolyzer by coupling the cathodic NtrRR and anodic hydrazine oxidation reaction (Fig. S13, ESI†).²³ Hydrazine (N_2H_4) is widely distributed in industrial wastewaters such as pharmaceuticals, dyes, and rubber, *etc.* We used RuO_x as the anode catalyst and $\text{H}_\text{o}\text{-Fe}_2\text{O}_3$ as the cathode catalyst. The batteryolyzer shows a maximum discharge power density of up to 2.85 mW cm^{-2} at the current density of 18 mA cm^{-2} (without IR correction, Fig. 4a). This device can generate power continuously for at least 25 000 s at 10 mA cm^{-2} (Fig. 4b). In short, the batteryolyzer proposed in this study provide an alternative and promising green approach for practical ammonia production and sustained power output.

In conclusion, we demonstrated the crystal facet-dependent NtrRR performance of non-noble metal Fe_2O_3 catalysts.

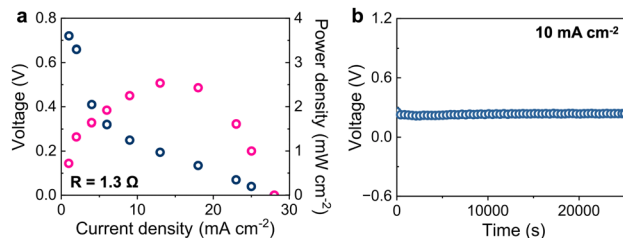


Fig. 4 (a) Polarization and power density curves, and (b) long-term chronopotentiometry curve under 10 mA cm⁻² output of a N₂H₄-nitrate battery.

Specifically, we showed that the H₀-Fe₂O₃ catalyst with high-index (13–44) and (12–38) facets exhibits optimal NtrRR activity and selectivity, achieving a high faradaic efficiency of up to 96.54% and an ammonia production rate of up to 1.13 mmol h⁻¹ cm⁻² at 250 mA cm⁻². In addition, the developed catalysts enabled the N₂H₄-nitrate battery to generate electricity at a high power density of 2.85 mW cm⁻², with sustained nitrate-to-ammonia conversion. Our work not only establishes H₀-Fe₂O₃ as a highly active non-noble metal NtrRR electrocatalyst, but also highlights the important role of high-index facets in improving electrocatalytic performance.

This work was supported by the Natural Science Foundation of Xiamen, China (Grant No. 3502Z202473021) and the Fundamental Research Funds for the Central Universities of China (Grant No.: 20720240066).

Data availability

The data supporting this article have been included as part of the ESI.†

Conflicts of interest

There are no conflicts to declare.

Notes and references

- 1 A. Valera-Medina, H. Xiao, M. Owen-Jones, W. I. F. David and P. J. Bowen, *Prog. Energy Combust. Sci.*, 2018, **69**, 63–102.
- 2 V. Kyriakou, I. Garagounis, A. Vourros, E. Vasileiou and M. Stoukides, *Joule*, 2020, **4**, 142–158.
- 3 C. Smith, A. K. Hill and L. Torrente-Murciano, *Energy Environ. Sci.*, 2020, **13**, 331–344.
- 4 Y. W. Ren, C. Yu, X. Y. Tan, Q. B. Wei, Z. Wang, L. Ni, L. S. Wang and J. S. Qiu, *Energy Environ. Sci.*, 2022, **15**, 2776–2805.
- 5 G. Soloveichik, *Nat. Catal.*, 2019, **2**, 377–380.
- 6 J. Wang, T. Feng, J. X. Chen, V. Ramalingam, Z. X. Li, D. M. Kabtamu, J. H. He and X. S. Fang, *Nano Energy*, 2021, **86**, 17.
- 7 X. Fu, *Chin. J. Catal.*, 2023, **53**, 8–12.
- 8 W. D. Chen, X. Y. Yang, Z. D. Chen, Z. J. Ou, J. T. Hu, Y. Xu, Y. L. Li, X. Z. Ren, S. H. Ye, J. S. Qiu, J. H. Liu and Q. L. Zhang, *Adv. Funct. Mater.*, 2023, **33**, 23.
- 9 Z. X. Wang, S. D. Young, B. R. Goldsmith and N. Singh, *J. Catal.*, 2021, **395**, 143–154.
- 10 W. Zhu, F. Yao, Q. Wu, Q. Jiang, J. Wang, Z. Wang and H. Liang, *Energy Environ. Sci.*, 2023, **16**, 2483–2493.
- 11 J. Lim, C.-Y. Liu, J. Park, Y.-H. Liu, T. P. Senftle, S. W. Lee and M. C. Hatzell, *ACS Catal.*, 2021, **11**, 7568–7577.
- 12 Y. Yao, L. Zhao, J. Dai, J. Wang, C. Fang, G. Zhan, Q. Zheng, W. Hou and L. Zhang, *Angew. Chem., Int. Ed.*, 2022, **61**, e202208215.
- 13 Q. Wu, W. Zhu, D. Ma, C. Liang, Z. Wang and H. Liang, *Nano Res.*, 2024, **17**, 3902–3910.
- 14 T. Li, C. Tang, H. Guo, H. Wu, C. Duan, H. Wang, F. Zhang, Y. Cao, G. Yang and Y. Zhou, *ACS Appl. Mater. Interfaces*, 2022, **14**, 49765–49773.
- 15 Z. Hou, Y. Zhang, H. Chen, J. Wang, A. Li and P. François-Xavier Corvini, *Small*, 2024, **20**, 2406424.
- 16 S. D. Sun, X. Zhang, J. Cui, Q. Yang and S. H. Liang, *Nanoscale*, 2019, **11**, 15739–15762.
- 17 H. Liang, W. Chen, R. Wang, Z. Qi, J. Mi and Z. Wang, *Chem. Eng. J.*, 2015, **274**, 224–230.
- 18 C. S. Wang, Q. Zhang, B. Yan, B. You, J. J. Zheng, L. Feng, C. M. Zhang, S. H. Jiang, W. Chen and S. J. He, *Nano-Micro Lett.*, 2023, **15**, 41.
- 19 J. Wang, Y. Q. Zhang, S. J. Jiang, C. Z. Sun and S. Q. Song, *Angew. Chem., Int. Ed.*, 2023, **62**, 7.
- 20 M. Zhao and H. Liang, *ACS Nanosci. Au*, 2024, **4**, 409.
- 21 S. Mondal, S. Sarkar, D. Bagchi, T. Das, R. Das, A. K. Singh, P. K. Prasanna, C. P. Vinod, S. Chakraborty and S. C. Peter, *Adv. Mater.*, 2022, **34**, 10.
- 22 Y. Zhang and H. Liang, *Chem. Synth.*, 2024, **4**, 39.
- 23 W. Zhu, X. Zhang, F. Yao, R. Huang, Y. Chen, C. Chen, J. Fei, Y. Chen, Z. Wang and H. Liang, *Angew. Chem., Int. Ed.*, 2023, **62**, e202300390.
- 24 H. F. Liang, X. D. Jiang, Z. B. Qi, W. Chen, Z. T. Wu, B. B. Xu, Z. C. Wang, J. X. Mi and Q. B. Li, *Nanoscale*, 2014, **6**, 7199–7203.
- 25 X. Y. Yu, L. Yu, L. F. Shen, X. H. Song, H. Y. Chen and X. W. Lou, *Adv. Funct. Mater.*, 2014, **24**, 7440–7446.
- 26 P. G. He, Z. P. Ding, X. D. Zhao, J. H. Liu, S. L. Yang, P. Gao and L. Z. Fan, *Inorg. Chem.*, 2019, **58**, 12724–12732.
- 27 R. J. Angel, M. Murri, B. Mihailova and M. Alvaro, *Z. Kristallogr. – Cryst. Mater.*, 2019, **234**, 129–140.
- 28 X. Zou, J. Xie, C. Wang, G. Jiang, K. Tang and C. Chen, *Chin. Chem. Lett.*, 2023, **34**, 107908.
- 29 M. Karamad, T. J. Goncalves, S. Jimenez-Villegas, I. D. Gates and S. Siahrostami, *Faraday Discuss.*, 2023, **243**, 502–519.
- 30 Z. Shu, H. Chen, X. Liu, H. Jia, H. Yan and Y. Cai, *Adv. Funct. Mater.*, 2023, **33**, 2301493.
- 31 X. Zhang, X. Liu, Z.-F. Huang, L. Gan, S. Zhang, R. Jia, M. Ajmal, L. Pan, C. Shi and X. Zhang, *Energy Environ. Sci.*, 2024, **17**, 6717–6727.